Diffracted waves and displacement field over two-dimensional elevated topographies

Pierre-Yves Bard *Laboratoire de Géophysique Interne (associé au CNRS: ERA 603) IRIGM, Université Scientifique et Médicale de Grenoble BP 53X, 38041 Grenoble Cedex, France*

Summary. The Aki-Larner technique is used to perform, in both the time and frequency domains, an analysis of the effects of two-dimensional elevated topography on ground motion. Incident plane *SH*-, *SV*- and *P*-waves are considered and the respective influences of surface geometry, elastic parameters and the incident wave characteristics, as long as they remain within the limits of applicability of the A-L technique, are investigated in some detail.

Besides the well-known amplification/deamplification effect related to the surface curvature, wave scattering phenomena on the convex parts of the surface are shown to contribute significantly to the disturbances in the displacement field around the topographic structure. These scattered waves are *SH* in the case of incident *SH*-waves, and mainly Rayleigh waves in the *P* case, while both Rayleigh and horizontal *P*-waves, sometimes of large amplitude, develop in the *SV* case. The frequency dependence of this scattering, though complex, seems to be mainly controlled by the horizontal scale of the topographic structure. The parameter study points out the regular and intuitive behaviour of this wave scattering in both *SH* and *P* cases, while it exhibits a puzzling complexity for incident *SV*-waves, which is interpreted as resulting from the importance of the *S–P* reflections on mountain slopes in that case.

As to the ground motion, some general features may be pointed out. The amplification on mountain tops, which is systematically greater for incident *S*-waves than for *P*-waves, generally decreases as the average slope decreases or as the angle of incidence increases. Mountain slopes undergo either amplification or deamplification depending on site location, frequency and incidence angle, but they always undergo strong differential motion due to the lateral propagation of the scattered waves and their interference with the primary wave. Finally, all these effects may be greatly enhanced in the case of complex topographies, which moreover give rise to a significant prolongation of ground motion because of the large number of scattered waves.

1 Introduction

For many years, a great number of authors have pointed out the importance of site effects in many seismological problems, ranging from source parameter computation to seismic risk assessment. These site effects were at first related to the local sediment cover (resonance of surface layers, sand liquefaction, attenuation of high frequencies, etc.). More recently, however, observations have been made (e.g. Key 1967; Nason 1971; Trifunac & Hudson 1971) showing the influence of topography on surface ground motion.

Besides field studies (Davis & West 1973; Griffiths & Bollinger 1979), or model studies (Rogers, Katz & Bennett 1974; Ilan, Bond & Spivack 1979), the theoretical investigations have focused more on numerical solution rather than on a detailed study of the effects of topography on surface motion. A lot of numerical methods have been developed to investigate the scattered far-field (small perturbations: Gilbert & Knopoff 1960; Hudson & Knopoff 1967; Hudson 1967; MacIvor 1969; small perturbations and finite difference: Aboudi 1971; Alterman & Aboudi 1971), or the displacement field over the topography itself (analytical models: Trifunac 1973; Wong & Trifunac 1974; Singh & Sabina 1977; finite differences: Boore 1972; Alterman & Nathaniel 1975; Ilan 1977; Ilan *et al.* 1979; finite elements: Smith 1975; discrete wavenumber representation: Larner 1970; Bouchon 1973; matched asymptotic expansion: Sabina & Willis 1975, 1977; integral equations: Wong & Jennings 1975; Sills 1978; Sanchez-Sesma & Rosenblueth 1979; and boundary methods: England, Sabina & Herrera 1980). All these theoretical models, involving a two-dimensional homogeneous elastic half-space with a simple topographic section (except Singh & Sabina 1977, who consider a three-dimensional hemispheric valley), provide results which quantitatively agree with one another, and qualitatively confirm the experimental observations: amplification usually occurs on convex parts of the ground surface (mountain tops or valley edges), and deamplification on concave parts and shadow zones. Our purpose here is therefore not to present yet another numerical method, but to try to gain a better understanding of these topographic effects, through their dependence on parameters such as incident wave type, frequency, incidence angle and anomaly height.

In other respects, all available theoretical results seem to underestimate the observed effects of topography on surface motion, as reported by Davis & West (1973), and Griffiths & Bollinger (1979). Since the model study values corroborate those obtained by numerical methods (Rogers *et al.* 1974; Ilan *et al.* 1979), it is believed that quantitative disagreement between theory and observation is due, at least partly, to the complexity of both incident signal and topography. It is therefore another aim of the present paper to show how a somewhat complicated topography can produce greater effects than isolated ridges or valleys, and that the surface motion at a particular site depends a lot on the topographic features of a wide area around.

We believe that the Aki-Larner method is the best suited to this kind of study, since it is a very tractable and computationally cheap method, and because the discrete wavenumber representation provides useful information on the nature of the scattered elastic field. This
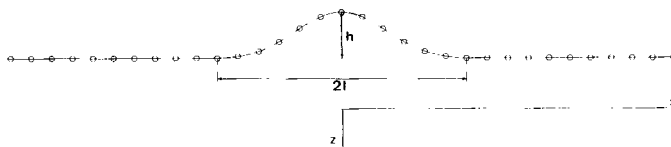

Figure 1. Geometrical shape of the mountain model introduced by Sills (1978), and corresponding to the cases investigated in Figs 2–17. The open circles indicate the sites where the synthetic seismograms of Figs 2, 3 and 14 are computed.

technique has already been presented with many details by Larner (1970), Aki & Larner (1970) and Bouchon (1973), and its reliability carefully discussed. The limitation of our investigations to topographic features having slopes lower than 40°, and to incident body waves only, with rather small incidence angles so as to avoid shadow zones, together with the experimental observations of Rogers *et al.* (1974) and Ilan *et al.* (1979) showing that the radiation lobes of the diffracted waves are directed essentially downwards, allow us to think that the Rayleigh ansatz error does not alter the accuracy of our results too much.

2 Effects of simple topography on incident plane waves – a parameter study

2.1 GENERALITIES

Our purpose is to evaluate the surface displacement and the scattered elastic field produced by a plane body wave impinging upon a two-dimensional topographic feature lying over an otherwise isotropic homogeneous elastic half-space, for various topography, half-space and incident wave characteristics.

Our computations rely on the same theoretical formulation as those presented by Bouchon (1973), except that we do not correct the displacement field for the residual stresses, since we remain well within the validity limits of the A-L technique. Furthermore, in order to investigate the ground motion in the time domain, we follow the approach described by Bard & Bouchon (1980a), making the computation at equally spaced frequencies having an imaginary part equal to half the frequency step. The disturbances induced by the structure periodicity L (required by the A-L method) are avoided by a suitable choice of both the frequency range and the time window.

Topographic effects then depend on three kinds of parameters:

2.1.1 *Topographic shape*

This is the most difficult to quantify. For a better understanding of the diffraction and amplification/deamplification mechanisms, only simple topographic profiles are considered at first. The 'pseudo-realistic' mountain model of Sills (1978) is chosen, defined through the equation:

$$\zeta(x) = h(1 - a) \cdot \exp(-3a) \qquad \text{with} \qquad a = (x/l)^2$$

this topography is completely defined by its half-width l and its height h. Its shape is illustrated in Fig. 1.

2.1.2 *Half-space elastic parameters*

These reduce to the shear and compressional velocities, respectively denoted as β and α, since the material density has no influence.

2.1.3 *Incident wavefield characteristics*

These are wave type, incidence angle, azimuth and frequency spectrum. Only incident plane waves are considered here, for simplicity and because nearfield studies introduce a lot of new parameters related to the source mechanism. Moreover, only incident body waves are taken into account. The effect of incident wave azimuth is not considered: only in plane and out of plane motions are investigated.

The remaining independent dimensionless parameters considered in this paper are therefore: the topography shape ratio h/l, the Poisson ratio ν, the dimensionless frequency

$\eta = 2l/\lambda$ (which is scaled to the S wavelength $\lambda = \beta/f$), and the incidence angle θ, measured from the vertical axis.

For time domain studies, we generally choose an input signal in form of a Ricker wavelet, having a time dependence:

$$f(t) = (a - 0.5)\exp(-a) \qquad \text{with} \qquad a = |\pi(t - t_s)/t_p|^2$$

where t_s is the time of maximum amplitude, and t_p the characteristic period. We also sometimes use a combination of several Ricker wavelets.
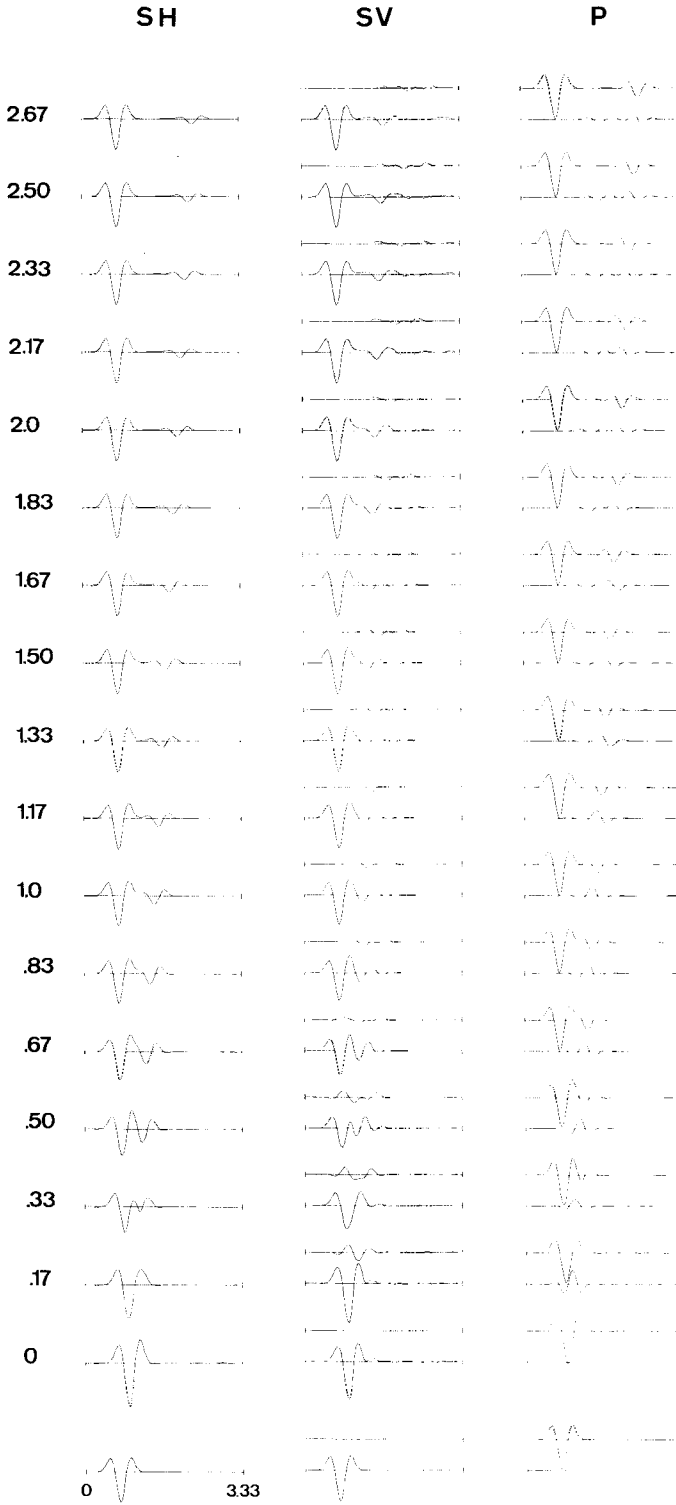
2.2 GENERAL CHARACTERISTICS OF TOPOGRAPHIC EFFECTS IN THE VERTICAL INCIDENCE CASE

In this section the case of P, SV and SH plane waves vertically incident on two topographic features is investigated, a mountain having a shape ratio h/l equal to 0.375, and a symmetric depression. Materials with Poisson's ratio $v = 0.25$ are considered until Section 2.5.

2.2.1 Time domain study

Fig. 2 illustrates the time history of ground motion at several sites located over the topographic elevation and some distance apart, for an incident Ricker signal having a characteristic dimensionless frequency of $\eta_p = 1.83$, in each of the three SH, SV and P incident cases. The well-known amplification pattern on mountain tops appears on each of the three components, but it is more important in the case of incident S-waves (43 per cent for SH and 30 per cent for SV) than in the case of incident P-waves (only 10 per cent). Moreover the computed motions do not exhibit much change in signal waveform or duration. On the contrary, on mountain slopes, significant alterations appear; while the ground displacement amplitude is reduced, its duration is increased. The amplitude reduction is more important for horizontal components (the maximum attenuation is about 25 per cent for SH, 40 per cent for SV and only 10 per cent for incident P-waves). In the SH case, seismograms away from the topography show an outward propagating signal having roughly the same shape as the incident signal and an amplitude of about 20 per cent at a distance $2l$ from the mountain top. The phase velocity of this diffracted wave, together with the space dependence of its amplitude, which fits an $x^{-1/2}$ decay, are consistent with a horizontal SH-wave generated near the mountain top. In the P and SV cases, seismograms exhibit a somewhat greater complication, because of the outward propagation of two such diffracted waves. Their phase velocities, vertical/horizontal component ratio, and spatial decay ($x^{-1/2}$ for the fastest wave, and nearly constant for the slowest), allow their identification as a horizontal P-wave and Rayleigh wave, respectively. The relative importance of these two waves undergoes great changes with the incident wave type. In the SV case, the horizontal P-wave is the main disturbance and is associated with a horizontal displacement around 20 per cent of the direct one (measured at the same reference site $x = 2l$), whereas in the P case,

Figure 2. Response of the mountain illustrated in Fig. 1 (h/l = 0.375) to vertically incident, respectively, SH, SV and P Ricker wavelets of characteristic dimensionless frequency η_p = 1.83. The traces represent the time history of the displacement at surface receivers, spaced from 0 to $2.5l$ from the mountain top (numbers on the left represent the site location in dimensionless values x/l). In the SH case, only the transverse horizontal component, v, is represented, while in the P and SV cases, both horizontal motion along the x-axis (u, lower trace) and vertical motion (w, upper trace), are depicted. The bottom traces represent the ground motion for a plane free surface. The dimensionless length of the time window is 3.33. Here v = 0.25.

SH **SV** **P**

2.67

2.50

2.33

2.17

2.0

1.83

1.67

1.50

1.33

1.17

1.0

.83

.67

.50

.33

.17

0

0   3.33

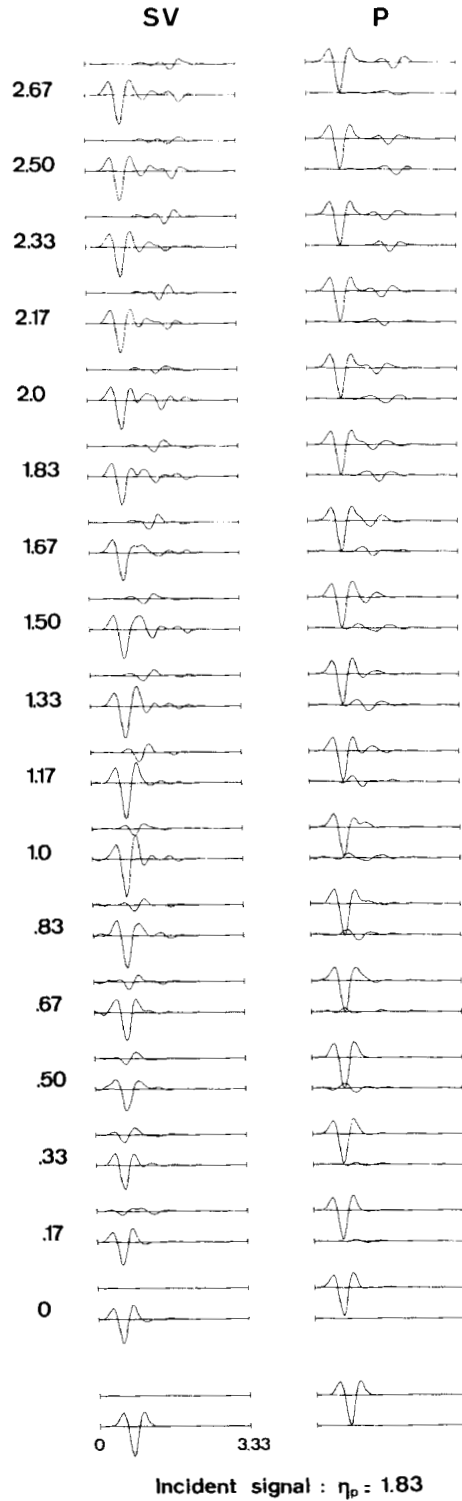**Incident signal : η_p = 1.83**

Figure 3. The same as Fig. 2, but for a depression of same shape ratio. Only the SV and P cases are illustrated.

the most important disturbance is the Rayleigh wave, which produces a vertical displacement around 25 per cent of the direct one. The deamplification pattern at the mountain base, reported by some authors, does not show up here, probably because the incident signal has a relatively short duration, so that direct signal and diffracted waves are well separated and do not interfere. On the contrary, the crest/flank amplification ratio reaches rather large values for incident *S*-waves (2 in the *SH* case, 2.2 in the *SV* one).

The case of *P*- and *SV*-waves vertically incident on a depression is illustrated in Fig. 3. The bottom of the canyon undergoes deamplification in both cases, the amount of which is greater on the horizontal (20 per cent) than on the vertical motion (10 per cent). The synthetic seismograms on canyon flanks exhibit only a slight deamplification in the *SV* case, and no changes as to signal duration and waveform. On the contrary, the ground motion at sites distant from the valley borders reveals an outward propagation of diffracted waves generated at the valley edges, which themselves undergo a clear amplification (around 20 per cent for incident *SV*-waves).
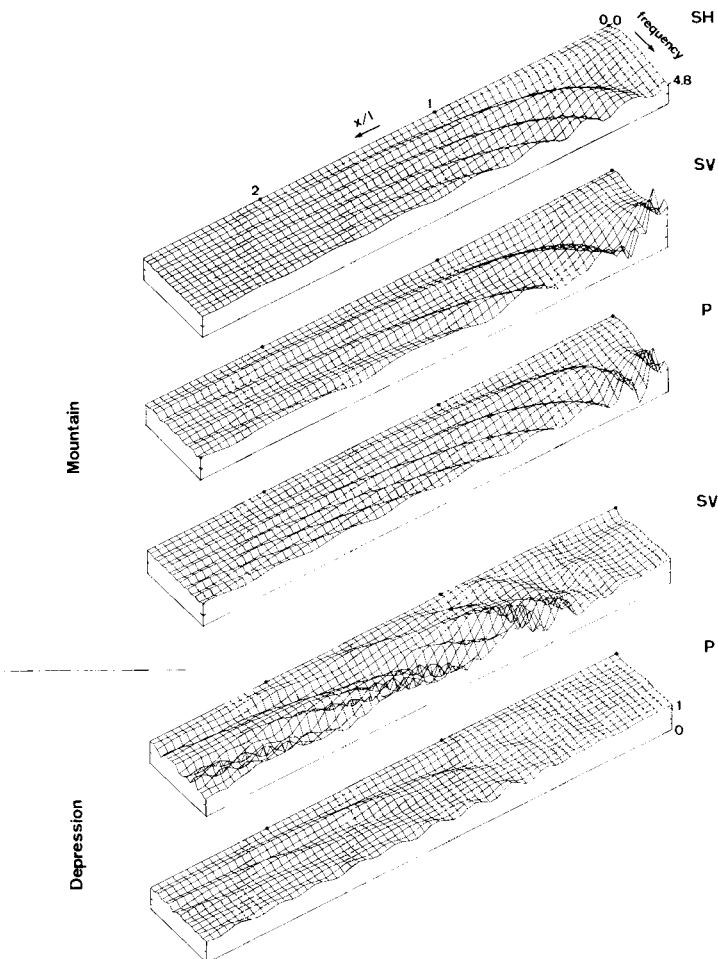

Figure 4. Amplitude of the ground motion as a function of site location and frequency. The three upper diagrams depict the mountain case (Fig. 2) and the two lower the depression case (Fig. 3). The top diagram represents the horizontal transverse component v for the *SH* case, the second and fourth one the horizontal component u in the *SV* case, and the third and fifth the vertical component in the *P* case. The nul amplitude reference and the scale are indicated for each diagram. The topographic outline is not shown so as to see the displacement amplitude variations better.

26

2.2.2 Frequency domain study

It is important to get an idea of the frequency at which topographic effects (amplification or deamplification, diffraction of scattered waves) become significant. Theoretical calculations of Gilbert & Knopoff (1960), Hudson (1967) and Hudson & Boore (1980) relate the amplitude of the diffracted wave with the spatial Fourier transform of the topographic cross-section, so that this 'starting frequency' depends, for a given topographic shape, essentially on its width (in comparison to the wave velocity), while the shape ratio acts as an amplitude factor. Furthermore, experimental observations (Rogers *et al.* 1974) and theoretical computations (Boore 1972; Bouchon 1973) show surprisingly low values for these starting frequencies. On mountain tops, there appear spectral amplifications greater than 10 per cent for wavelengths about four times the total width of the topographic feature. Though our purpose here was not to investigate in detail the very low frequency domain, we may note that, for incident *P*- and *SV*-waves as well as for *SH*-waves, our computations happen to confirm these very low values of the 'starting frequency', and its main control by the topographic width (see Fig. 8b).

However, our interest here is in the 'medium frequency' domain, i.e. wavelengths between 2 or 3 times the mountain width, and its height. Fig. 4 represents the 'raw' displacement spectra in the *SH, SV* and *P* cases corresponding to Figs 2 and 3 (these are not the true displacement spectra because they must be corrected for the complex frequency, which attenuates the amplitude on elevated sites and lessens the importance of late arrivals). The low-frequency behaviour is consistent with the time domain observations reported
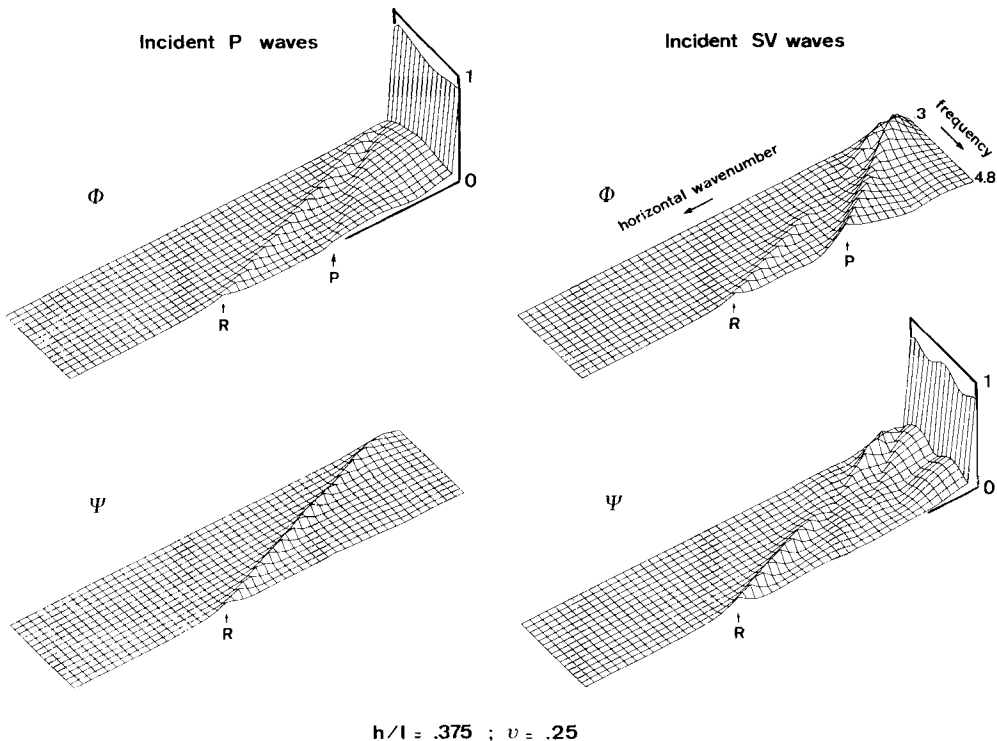

h/l = .375 ; υ = .25

Figure 5. Elastic potential characteristics for the topographic structure illustrated in Fig. 1, impinged by vertical *P*-waves (left) and *SV*-waves (right). The compressional (ϕ) and rotational (ψ) potentials of the scattered waves, computed at a z = 0 altitude, are shown as a function of frequency (dimensionless step: 0.3). *L* is the structure periodicity involved by the use of the A-L technique. The scale on the right of the upper left and bottom right diagrams represents the amplitude of the incident *P*- or *SV*-waves, respectively.

above, but higher frequencies give rise to significant changes, essentially on mountain slopes and valley edges; these changes follow an oscillatory pattern, due to the interaction between the direct and diffracted waves, as noted by Rogers *et al.* (1974). At a given site, the frequency spacing of lobes of constructive and destructive interference is inversely proportional to the time delay between the direct wave and the main diffracted wave. For instance, the frequency spacing at the same site is larger on the horizontal displacement for incident *SV*-waves than on the vertical one for incident *P*-waves, since the former is controlled mainly by the horizontally diffracted *P*-wave, and the latter by the Rayleigh wave. It is thus very difficult to predict whether amplification or deamplification will occur systematically at a given site; nevertheless, a constant feature is that mountain slopes always undergo strong differential strains, the amount of which increases with the frequency (at least within the frequency range investigated here).

On another hand, these oscillations converge towards the onset site of the corresponding diffracted waves. Fig. 4 thus indicates that the scattered *SH*-, *P*- and Rayleigh-waves originate at mountain tops and valley edges, that is, on convex parts of the topography. Also noticeable on this figure are the great high-frequency disturbances appearing in the horizontal
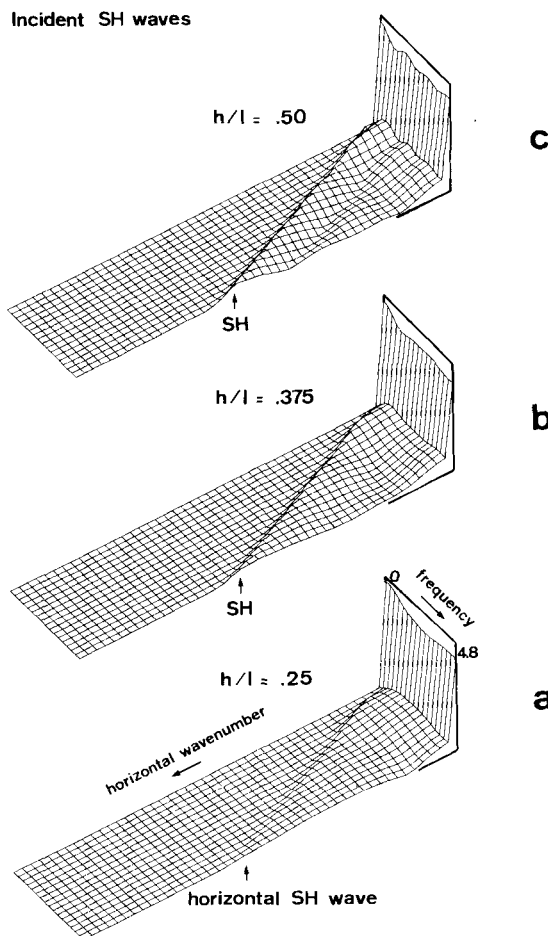

Figure 6. Variations of the scattered wavefield characteristics with the shape ratio in the *SH* case. The diagrams represent the amplitude of the scattered waves, computed at a $z = 0$ altitude, as a function of the horizontal wavenumber and of the frequency. These amplitudes are normalized to that of the incident wave.

displacement field for the canyon case. They are due to the Rayleigh ansatz error, which should be greatly reduced in more realistic models, where the presence of other interfaces would allow the presence of an upgoing diffracted field. However, in this paper, we have focused our interest on elevated topographic features, for which the Rayleigh ansatz error is rather small and localized.

The diagrams in Figs 5 and 6(b) illustrate the dependence of the scattered elastic field (represented by the elastic potentials ϕ and ψ in the P and SV cases, and the displacement in the SH case, each being computed at a $z = 0$ altitude) on both horizontal wavenumber and frequency. This scattered field is clearly separated into a main vertically reflected wave, homogeneous waves corresponding to the rays obliquely reflected on mountain slopes, and the horizontally diffracted SH-, P- and Rayleigh-waves. Although it is very difficult to distinguish between a horizontal SV-wave and a Rayeligh wave because of their small velocity difference, our opinion is that only a very small amount of energy is diffracted as a pure horizontal SV-wave, since the ψ/ϕ amplitude ratio, which is about 1.5 for the slowest branch, fits very well the theoretical Rayleigh curve (1.47 for $\nu = 0.25$). The amplitudes of both the vertically reflected wave and the oblique ones exhibit a quite strong dependence on frequency, but, in each case, minima of the vertical waves correspond to maxima of the homogeneous waves. Such a pattern suggests that the amount of energy propagating downwards remains roughly constant whatever the frequency. As to the waves diffracted along the surface, their amplitude does not depend strongly on the frequency, except for the Rayleigh wave in the SV incident case, which vanishes for dimensionless frequencies between 1.5 and 2.4. The reasons for this disappearance are not yet clear, but it explains the weakness of the Rayleigh wave on Fig. 2 in the SV incident case. Nevertheless, for other frequencies, the diffracted Rayleigh wave is larger for incident SV-waves than for incident P-waves, especially in the low-frequency domain. On another hand, the horizontal P-wave is almost non-existent in the P incident case.

As a partial conclusion, the topographic effects may be summarized as follows: the energy of the incident plane waves is first focused on convex parts of the surface topography where the displacement amplitude undergoes significant amplification over a rather broad frequency range. Although a large amount of this energy is reflected downwards as vertical and oblique homogeneous waves, the differential motion and strain induced by this local amplification make these convex parts radiate energy outwards in the form of surface waves (Rayleigh waves or surface SH- and P-waves). The fact that the mountain or valley slopes of the topographic feature investigated in this section, remain lower than $30°$, and thus cannot reflect SH and P incident rays into horizontal waves, which we nevertheless observe, supports this idea. Furthermore, the large amplitude of the horizontal P-wave in the SV incident case may result from the superposition of a classical geometric reflection of incident SV-waves on mountain slopes, and of this radiation from mountain tops. Therefore, except on mountain tops and valley bottoms where no diffracted waves arrive in the case of a single topographic feature, and where the displacement amplitude is thus mainly controlled by focusing or defocusing, the amplitude spectra are strongly governed by the interference between the direct and diffracted waves.

2.3 EFFECT OF MOUNTAIN HEIGHT

We consider in this section the case of plane SH-waves vertically incident upon two mountains having respective shape ratios 0.25 and 0.5, and the case of P- and SV-waves incident upon this last mountain, and we compare them with the results obtained in the previous section $(h/l = 0.375)$. The corresponding horizontal wavenumber frequency diagrams are shown in Fig. 6 for the SH case, and Fig. 7 for the P and SV cases (see Fig. 5 for comparison).

Incident P waves   **Incident SV waves**
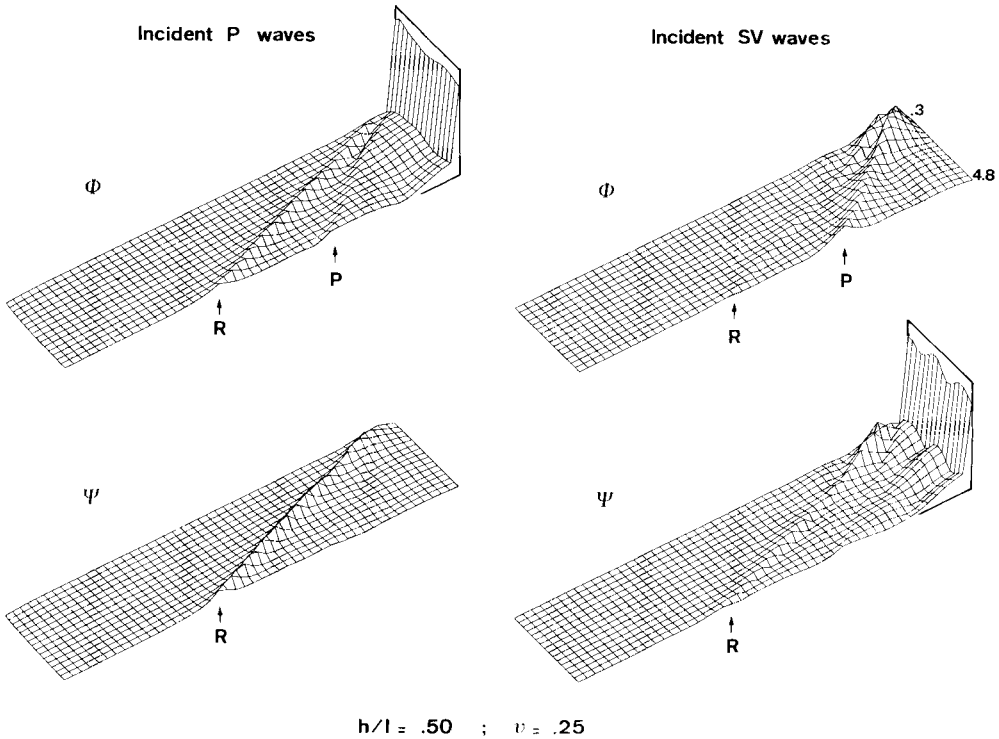

$h/l = .50$; $v = .25$

Figure 7. The same as Fig. 5, but for a higher elevation ($h/l = 0.50$).

2.3.1 Diffracted wavefield

The coupled frequency dependence of vertically and obliquely reflected waves mentioned above appears to be controlled by the mountain height: the frequency spacing of adjacent lobes gets narrower as the height increases. This phenomenon is interpreted as an interference scheme between vertical or subvertical waves reflected on the mountain top, and those reflected on each flat side of the topography. Such a hypothesis is supported by the measurement of the frequency spacing, which corresponds to a travel-time difference around $2\ h/c$, where c is the adequate wave velocity (β for incident S-waves, α for incident P-waves). This interference pattern has only little influence on the surface displacement, and has most effect on the deep underground motion below the topographic feature.

The horizontal diffracted SH-wave clearly strengthens as mountain height increases. Its amplitude is about 20—30 per cent larger for the highest elevation than for the medium-size one. This is only slightly lower than would result from a linear increase. Moreover, this ratio shows a trend to increase with frequency.

The horizontal P-wave scattered by incident P-waves also builds up as the shape ratio increases, but the Rayleigh wave still remains the most important feature. On the contrary, this regular strengthening is not observed in the SV incident case. The highest mountain scatters a greater amount of horizontal P-waves (up to 30 per cent more) only in the low-frequency domain, and the phenomenon is reversed for higher frequencies ($\eta > 3$).

The diffracted Rayleigh wave exhibits a behaviour very similar to that of the horizontal P-wave. In the incident P case, the Rayleigh wave shows a significant magnification (between 15 and 45 per cent) for the highest mountain and this magnification slightly increases with the frequency. On the other hand, for incident SV waves, the magnification (around 30 per
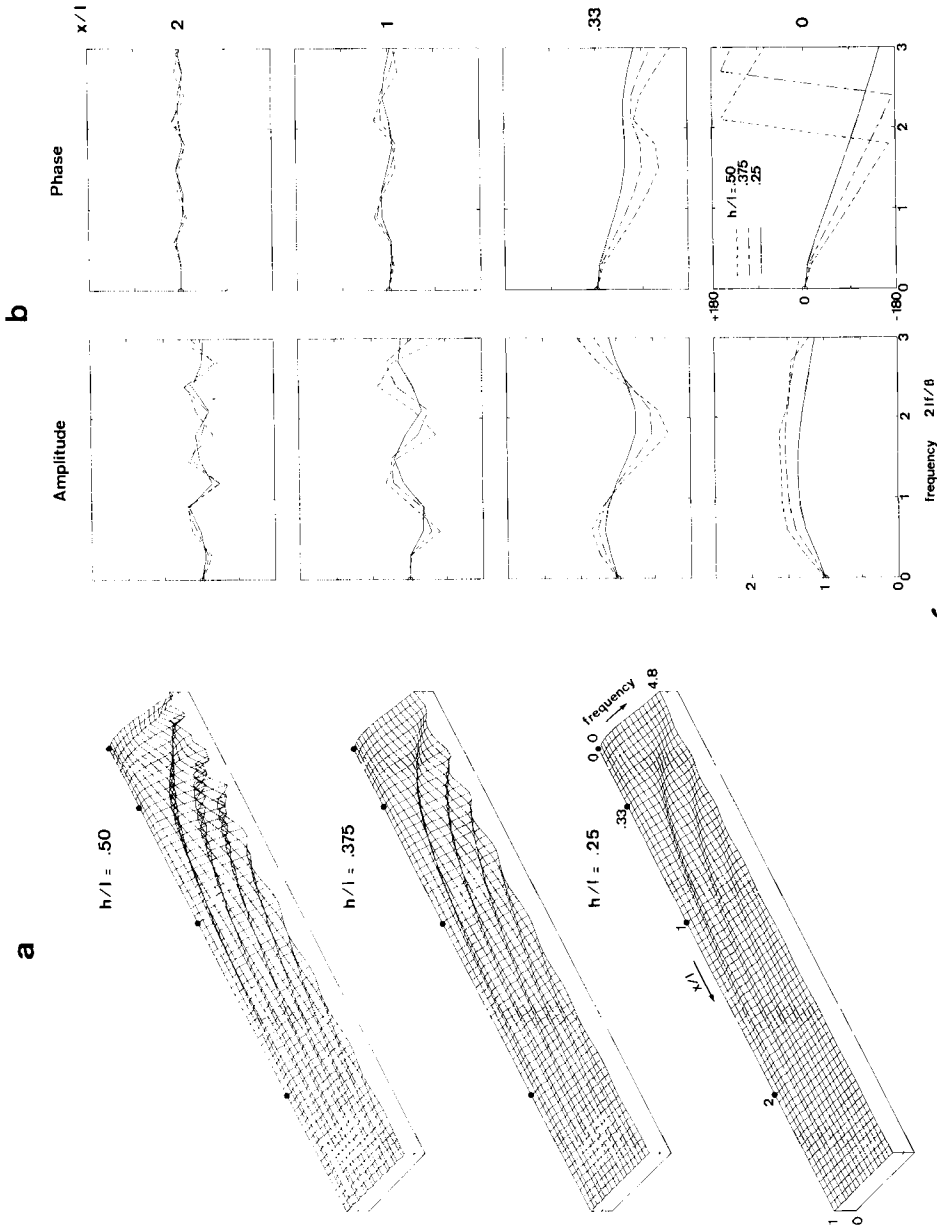
Figure 8. Variations of the displacement field with the shape ratio in the *SH* case. (a) Ground motion amplitude as a function of site location and frequency. (b) Detailed amplitude and phase spectra at four representative sites, the location of which is indicated by small dots on left diagrams.

cent) appears only at low frequencies ($\eta > 1.5$), and the trend is reversed for $\eta > 2.5$: higher elevations scatter less Rayleigh waves. The vanishing of the Rayleigh wave for dimensionless frequencies around 2 may be observed for both shape ratio values. This phenomenon therefore does not appear to be connected with the mountain height.

The regular strengthening, especially at high frequencies, of the wave scattering in both *SH* and *P* cases thus contrasts with its high-frequency weakening for incident *SV*-waves. Since this weakening does not occur at low frequencies, the reversal may be due, in our opinion, to the building up of horizontal interference phenomena within the mountain as both frequency and mountain height increase. It thereby must appear earlier in the *SV* case because of the *S–P* reflections on mountain slopes.

2.3.2 Displacement field

The frequency dependence of the displacement field in the *SH* incident case is shown in Fig. 8(a) for the three mountain heights. These diagrams bear obvious ressemblance to one another, except for the oscillatory pattern, the amplitude of which is related to the amplitude of the diffracted *SH*-wave. The amplitude spectra at four particular sites located on mountain crest, slope, base and some distance apart, are detailed on Fig. 8(b). As noticed above, the general shape of these spectra depends only slightly on mountain height, the main effect of which is to enhance the amplification or deamplification patterns. For instance, the maximum amplification on the mountain top is 36 per cent for the lowest, 53 per cent for the medium height and 65 per cent for the highest, in each case for a dimensionless frequency around 1.6; on another hand, the maximum deamplification on the mountain base is, respectively, 20, 30 and 42 per cent for dimensionless frequencies about 0.6.

It is interesting as well to look at the displacement phase versus frequency curves (Fig. 8b). For instance, the phase difference between mountain top ($x/l = 0$) and slope ($x/l = 0.33$) increases significantly for dimensionless frequencies around 1.8, and this increase enlarges with increasing mountain height. Such a phenomenon appears in a particularly strong way in the time domain, as shown in Fig. 9: the largest differential motions are concentrated around the site located at $x/l = 0.33$, and, for the highest mountain, the displacements on each side of this point are almost completely out of phase. Assuming for instance a 1 km wide, 250 m high hill, and a shear velocity of 3 km s^{-1}, these differential motions will act over a length of about 120 m for frequencies of about 6 Hz, that is within the frequency band of interest in earthquake engineering. Such differential motions may therefore be very important from an engineering point of view, as they may induce large torsional strain on big man-made structures.

2.4 SOME ASPECTS OF THE DEPENDENCE ON THE INCIDENCE ANGLE

Many authors have already investigated in some detail the displacement field over topographic features impinged upon by oblique and grazing *SH* plane waves (Trifunac 1973; Wong & Trifunac 1974; Wong & Jennings 1975; Sills 1978; Sanchez-Sesma & Rosenblueth 1979; England *et al.* 1980). Furthermore, a similar thorough investigation in the *P* and *SV* cases would need to be very fine, because of the great sensitivity of *P–SV* coupling on the incidence angle, especially in the *SV* case. Our aim here is therefore not to perform an exhaustive study of such a dependence, but only to give some indications about the qualitative and quantitative changes which may occur in the diffracted wavefield and ground displacement with varying incidence angle. We have thus investigated the elastic field scattered by a medium-size mountain ($h/l = 0.375$) illuminated by plane *SH*-waves with 30° and 60° incidence angles, and by *P*- and *SV*-waves at the critical angle $\theta = 35.68°$. This
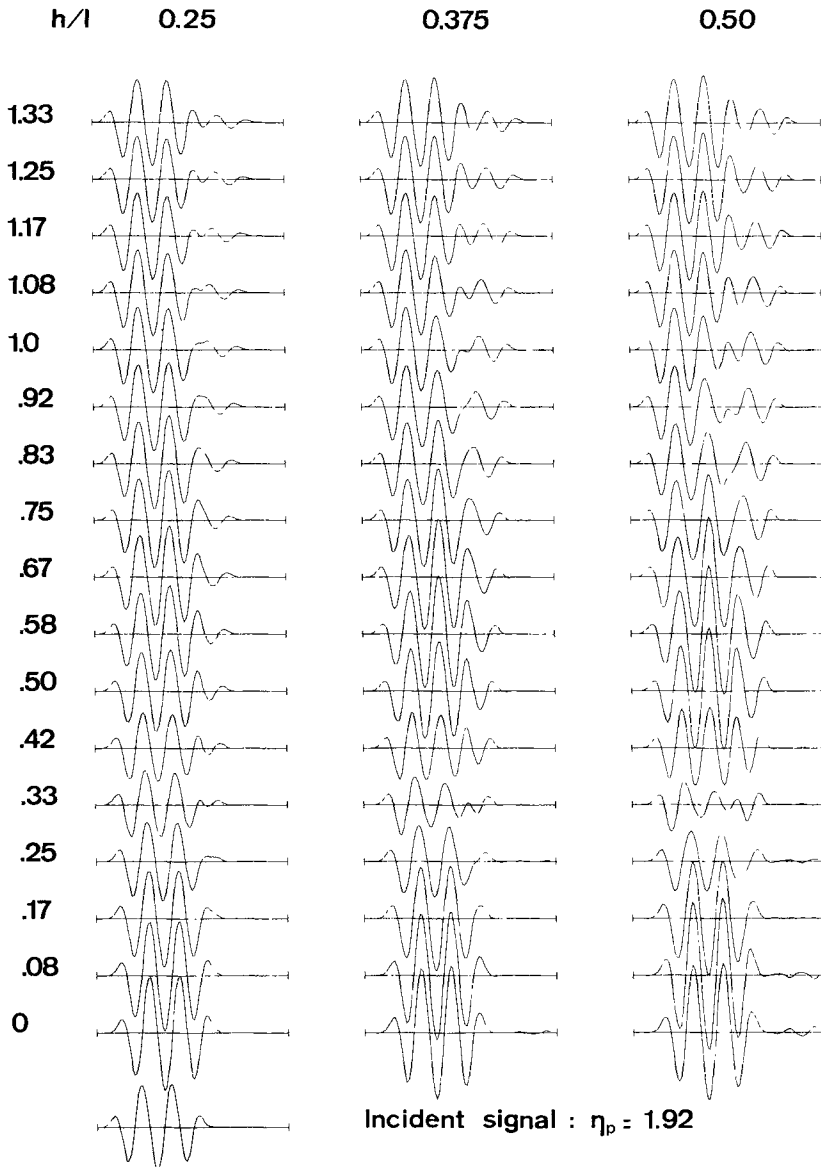
Figure 9. Dependence of ground motion on the shape ratio in the time domain. The incident signal is a combination of Ricker wavelets and is depicted by the bottom left trace. Numbers on the left are the dimensionless values of the horizontal distance between the recording site and mountain top.

particular value is chosen on the basis of our preliminary results (not reported here) which give evidence of a great enhancement of the forward scattered Rayleigh wave around this angle in the SV case, thus corroborating theoretical results obtained by Hudson & Knopoff (1967).

The most striking feature of the diffracted field is the directivity effect. In the SH case (Fig. 10), the forward scattered horizontal SH-wave exhibits an increase with respect to the vertical incidence case, which is about 100 per cent for $\theta = 30°$ and reaches 350 per cent for $\theta = 60°$. The P and SV cases (Figs 11 and 12) show the same qualitative behaviour for the
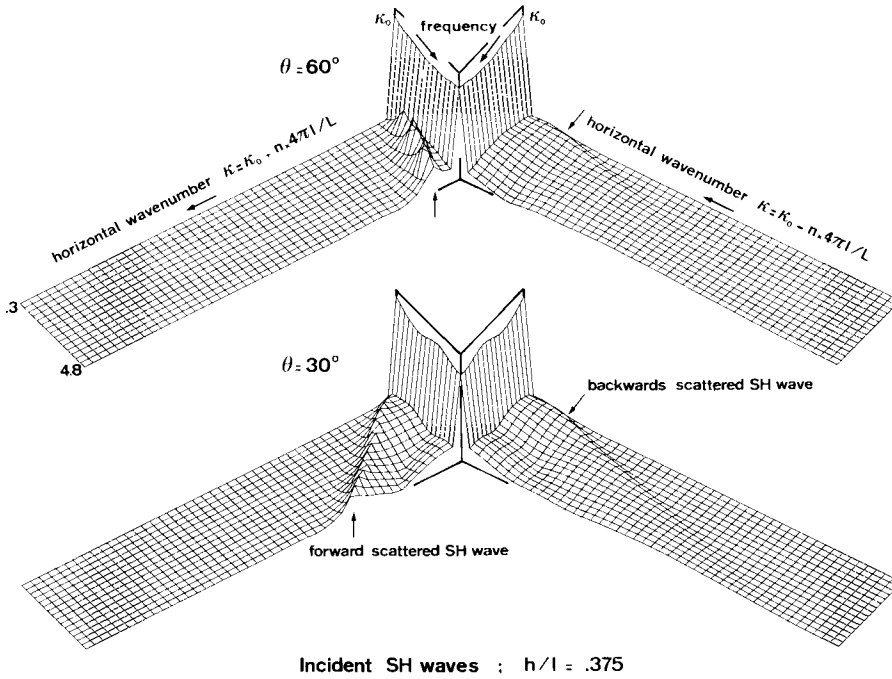
Figure 10. Variations of the scattered wavefield characteristics with the incidence angle in the *SH* case. These diagrams represent the amplitude of the scattered waves, computed at a $z = 0$ altitude, as a function of the horizontal wavenumber and of the frequency. The left part of the diagrams correspond to forward scattered waves, and the right one to the back scattered waves. K_0 is the horizontal wavenumber of the incident plane wave.
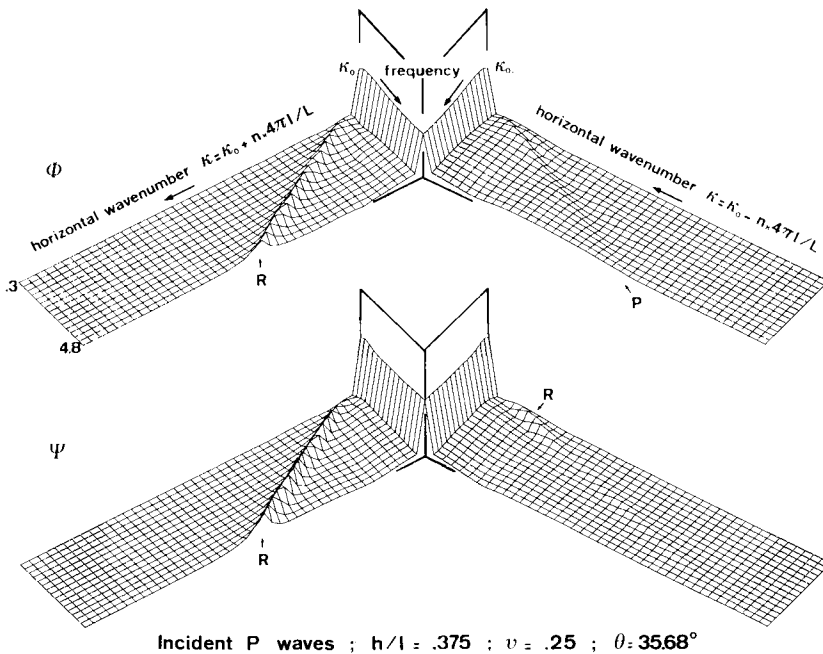
Figure 11. Elastic potential characteristics for obliquely incident *P*-waves. See Figs 5 and 10 for further explanations.

Incident **SV** waves ; h/l = .375 ; ν = .25 ; θ = 35.68°
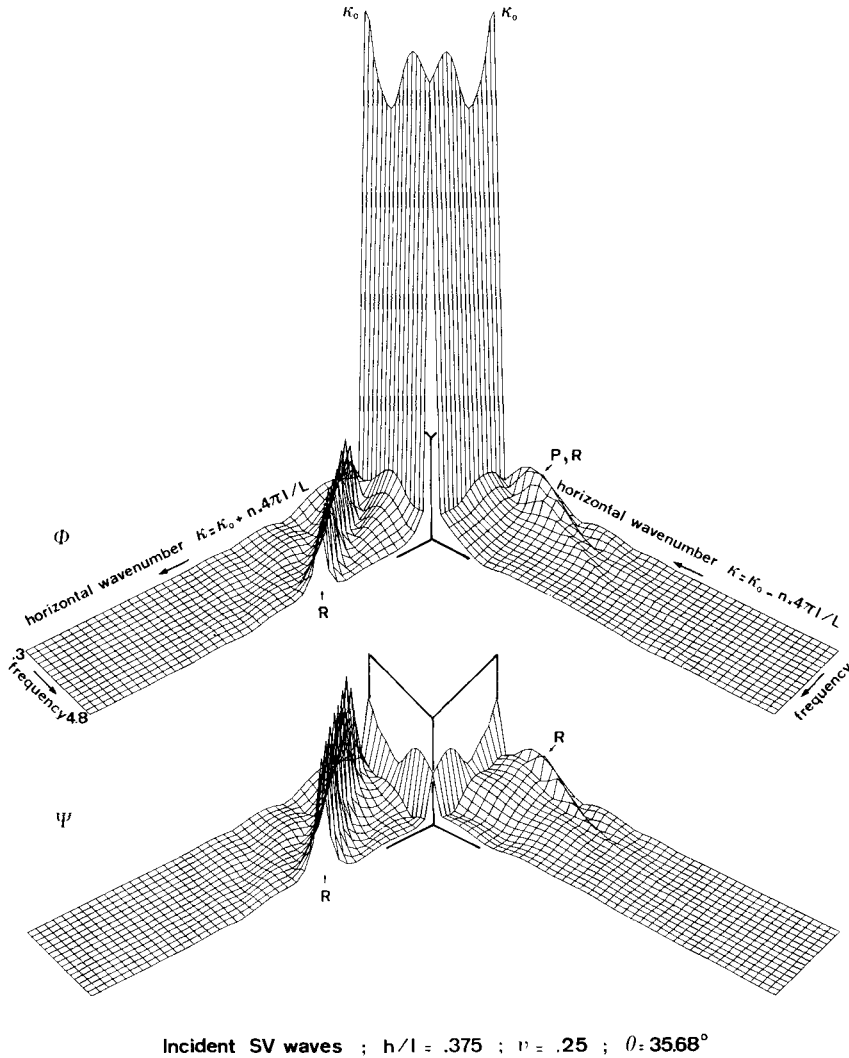
Figure 12. The same as Fig. 11, but for *SV*-waves incident at the critical angle. The scale is the same as in Fig. 11.

forward scattered Rayleigh wave; at that particular incidence angle, this enhancement is greatly emphasized in the *SV* case (Fig. 12), since it reaches one order of magnitude, while it ranges between 50 and 150 per cent in the *P* incident case. However, the ratio of the disturbance induced by the forward scattered Rayleigh wave to the surface displacement in the absence of the topographic feature is roughly the same in the two cases. Moreover, in each of the *SH, SV* and *P* cases, high frequencies seem to favour this enhancement of the forward scattered waves, and we may perhaps infer from the two *SH* diagrams (Fig. 10) that the frequency at which this reinforcement starts is greater for large incidence angles. Finally, for the particular *SV* case, the forward scattered Rayleigh wave no longer exhibits any vanishing or significant decrease for any frequency window. We do not observe any forward scattered *P*-wave in the *P* incident case.

For the back scattered field, we still observe a similar behaviour in each of the three cases, but quantitative values strongly differ from one another. The back scattered horizontal
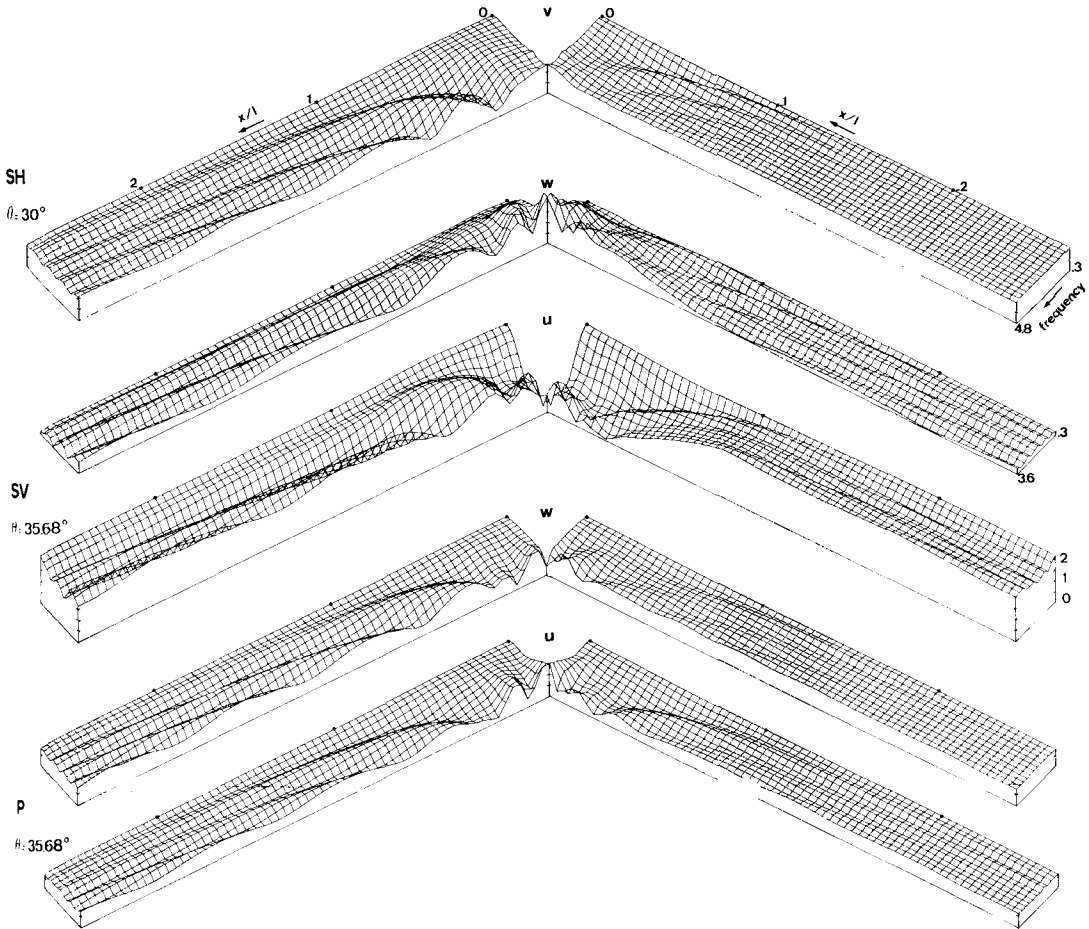
Figure 13. Ground motion amplitude as a function of frequency and site location, in, respectively, oblique *SH* (top diagram, transverse component *v*), *SV* (second, vertical component *w* and third digram, horizontal component *u*) and P cases (fourth, *w*, and fifth, *u*). The incident waves propagate in the positive *x*-direction, that is from right to left.

SH-, horizontal *P*- and Rayleigh-waves are essentially confined to the low-frequency domain, and this cut-off frequency seems to lessen as the incidence angle increases ($\eta \simeq 3.0$ for $\theta = 30°$, and $\eta = 1.2$ for $\theta = 60°$). But, whereas in the *SH* and *P* cases the amplitude of the corresponding back scattered waves is reduced a lot, except in the very low-frequency domain ($\eta < 0.6$) where it is only slightly lower than in the vertical incidence case, the amplitude of the back scattered waves in the *SV* case, for $\eta < 0.6$, is 300 per cent greater than in the vertical incidence case; the decrease with frequency is then very sharp, since the waves almost disappear for $\eta > 1.5$.

We may notice that these results are in good agreement with those of the small perturbation method: we have used the analytical formulation of Hudson (1967) to compute the amplitude of the Rayleigh wave scattered by the present mountain impinged by *P*- or *SV*-waves, and these calculations do predict both the strengthening of the forward scattered Rayleigh waves together with the high-frequency broadening of this scattering mechanism, and, concerning the back scattered Rayleigh wave, its confinement to lower frequencies together with its reduction in the *P* case and its amplification for *SV*-waves at critical angle.

The strengthening of the forward scattered Rayleigh wave in the P case is also consistent with experimental results of Rogers *et al.* (1974).

As for the surface displacement field (Fig. 13), we still observe that the most complicated case is the SV one. In both P and SH cases, the point of maximum amplification is slightly shifted away from the mountain top towards the 'far' side. The near side exhibits a main deamplification pattern, and the oscillation pattern on the far side is enhanced owing to the strengthening of the forward scattered waves. These features are conspicuously
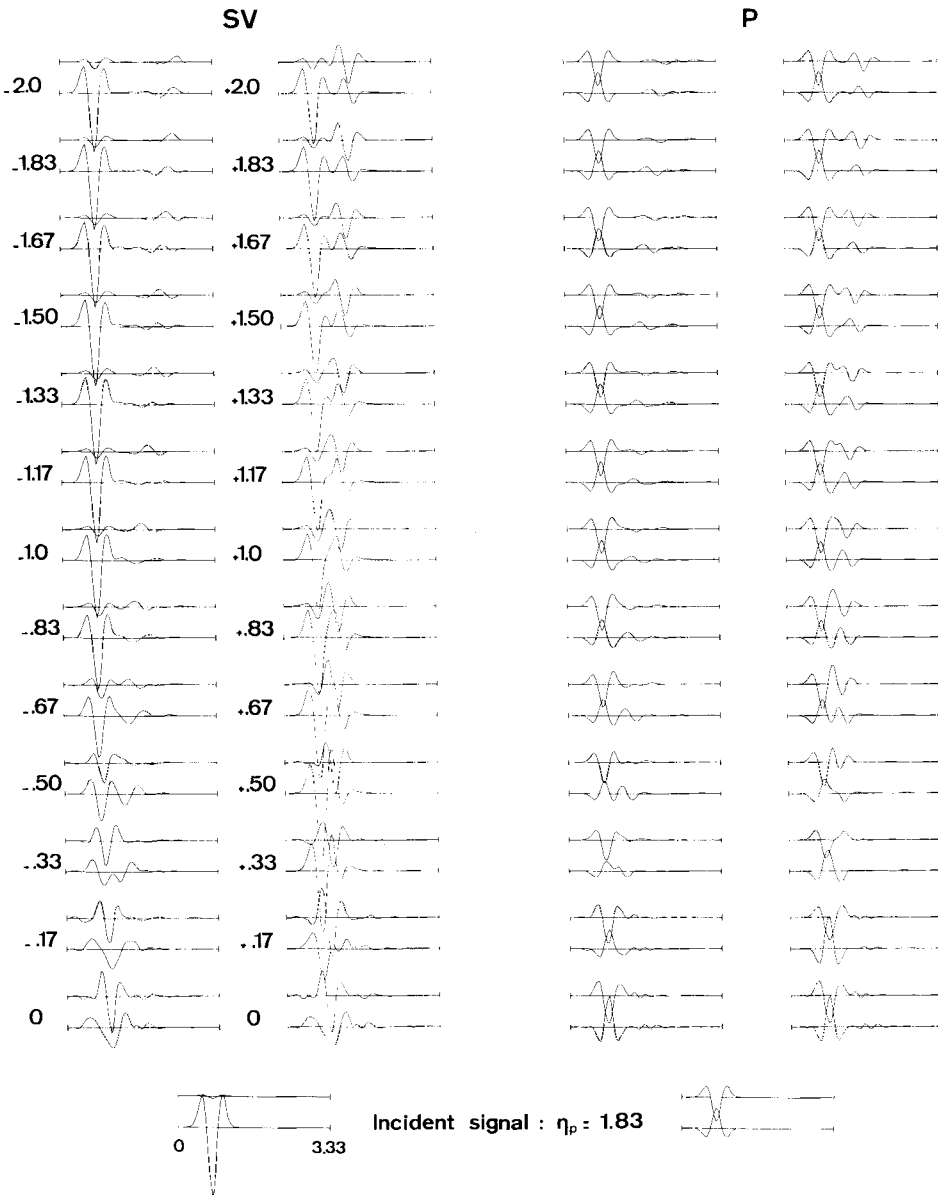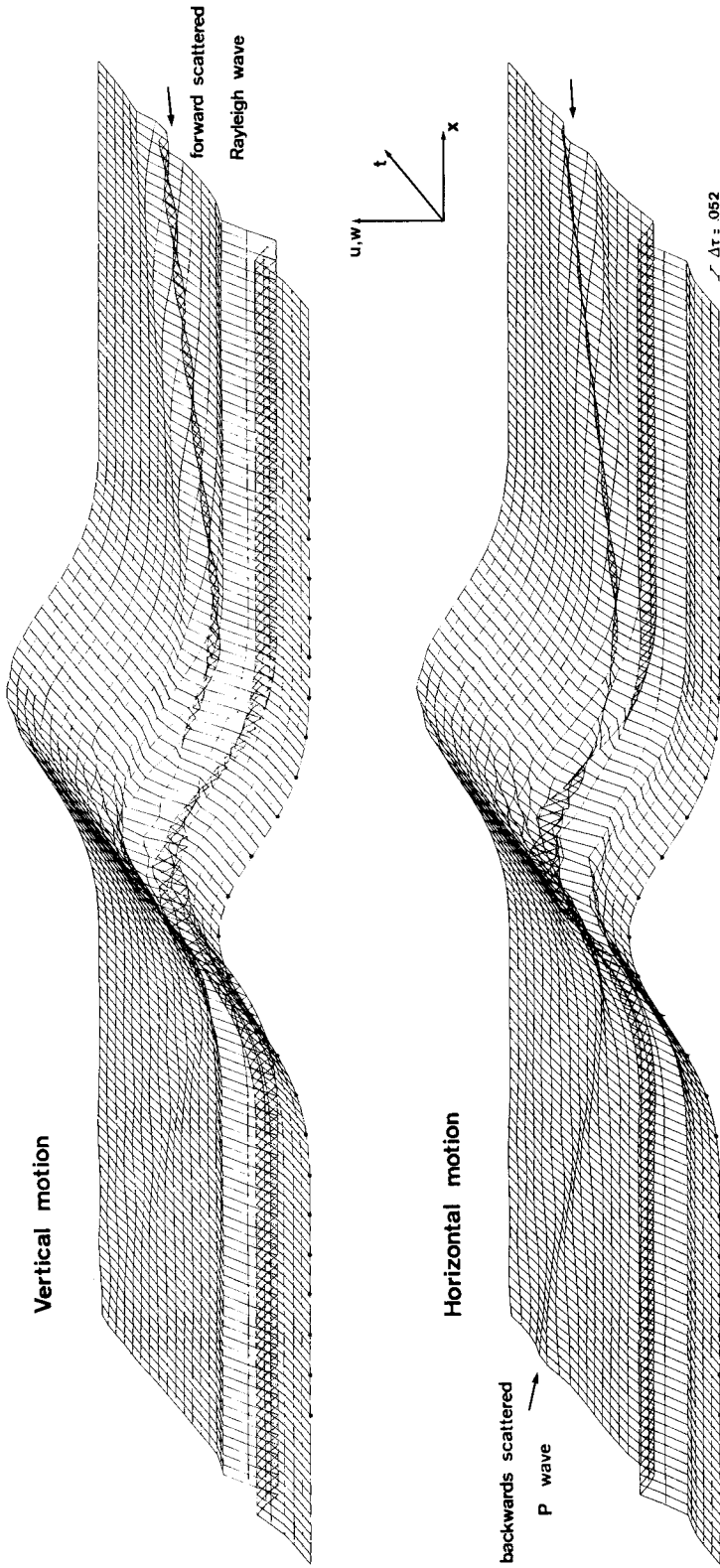
Figure 14. Time response of a medium-size mountain (h/l = 0.375) to obliquely incident (θ = 35.68°) SV and P Ricker wavelets of characteristic frequency 1.83. The bottom traces depict the ground motion for a plane free surface. Numbers on the left are the dimensionless values of the horizontal distance between the recording site and mountain top.

Figure 15. Spatial (x) and temporal (t) evolution of surface displacement components around a topographic structure impinged by oblique P-waves. The dots indicate the location of the sites where seismograms of Fig. 14 are computed.

Incident P waves ; h/l = .375 ; v = .25 ; θ = 3568°   Incident signal : η_p = 1.83

emphasized in the *SV* case. The deamplification pattern on the near side is combined with the great sensitivity of the surface horizontal displacement on the incidence angle (that is with the local surface slope), and, at low frequencies, with the interference between the back scattered Rayleigh and *P*-waves and the primary wave. The mountain top here exhibits a low frequency strong deamplification pattern, and the point of maximum amplification is located very near the middle of the slope. The vertical displacement is maximum near mountain top, and slightly greater on the far side than on the near one.

Synthetic seismograms in Fig. 14 provide a good illustration of all these features. The directivity effect appears very clearly for both *P* and *SV* cases. For instance, the forward scattered Rayleigh wave is five times larger than the back scattered one in the *SV* case. For incident *P*-waves, this ratio is greater since the back scattered Rayleigh is very weak. On the contrary, Fig. 15 shows a very clear back scattered *P*-wave, in this case, while there is no forward scattered such wave. The maximum displacement values undergo important changes over the topography, for both vertical and horizontal components in the *SV* case, and mainly for the horizontal component in the *P* case. As an example, the deamplification on the near side reaches 80 per cent in the *SV* case for the horizontal motion. An interesting feature is the motion at the mountain top in the *SV* case where horizontal or vertical components appear to be completely decoupled: the horizontal motion is of rather low frequency while the vertical motion attains much higher frequencies, and the apparent arrival time of the *SV*-wave is different on the two components (about 0.4 dimensionless time later on the vertical one).

2.5 ASPECTS OF THE INFLUENCE OF THE POISSON RATIO

The vast majority of Earth components have a Poisson ratio very near 0.25. Nevertheless, this value may be significantly greater for some surface materials, such as poorly consoli-
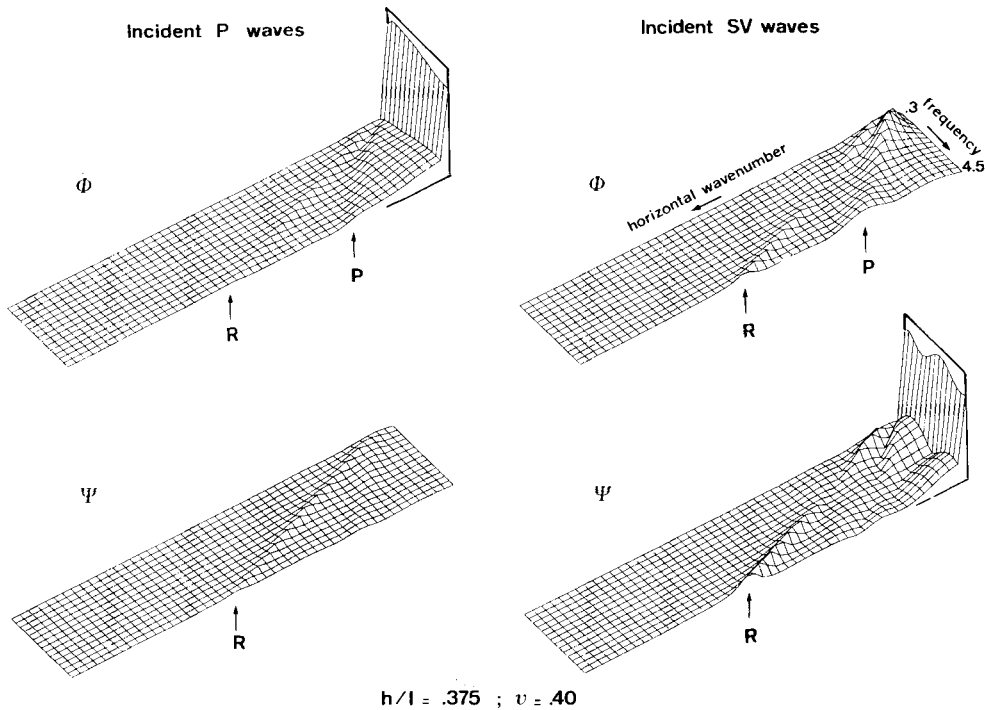

Figure 16. The same as Fig. 5, for a mountain of same shape but having a larger Poisson ratio, i.e. $\nu = 0.40$.

dated sediments or artificial fills. In order to get an idea of the upper limit of the changes in the diffraction and amplification/deamplification phenomena due to the Poisson ratio, we have investgated the case of a medium size mountain (h/l = 0.375) having a Poisson ratio of 0.40 (that is a shear to compressional velocity ratio of 0.41) impinged by vertical P- and SV-waves, for a dimensionless frequency up to 4.5.

As shown in Figs 16 and 17, these variations of the Poisson ratio induce significant variations on the scattered Rayleigh wave. For incident P-waves, its amplitude is much smaller for $\nu = 0.40$, especially at high frequencies: around one-half for $\eta < 2.5$, and one-third for $\eta > 3$. In the SV incident case, we observe a slight reduction too in the low frequency domain ($\eta < 1.5$), then the Rayleigh wave disappears, as in the $\nu = 0.25$ case, for dimensionless frequencies between 1.5 and 2.4, and, for higher frequencies, its amplitude is similar in both cases, and even a little greater for $\nu = 0.40$.

The horizontally diffracted P-wave is still very weak for incident P-waves, though slightly greater in the high Poisson ratio case. For incident SV-waves, its amplitude is comparable in both cases at dimensionless frequencies below 2.5, and it is then significantly lower (around one-half) in the high Poisson ratio case.

Also noticeable are a slight decrease in the amplitude of the homogeneous waves for low-frequency incident P-waves, and their opposite small increase for low-frequency incident SV-waves.

These variations in the diffracted field are obviously reverberating on the surface motion. At some distance from the topographic feature, the weakening of the main scattered waves (the P-wave for incident SV-waves, and the Rayleigh one in the P incident case), together with the slight increase in the amplitude of the other diffracted wave (respectively Rayleigh and P), somewhat lessen and disturb the oscillating pattern of the horizontal and vertical displacement spectra (Fig. 17).
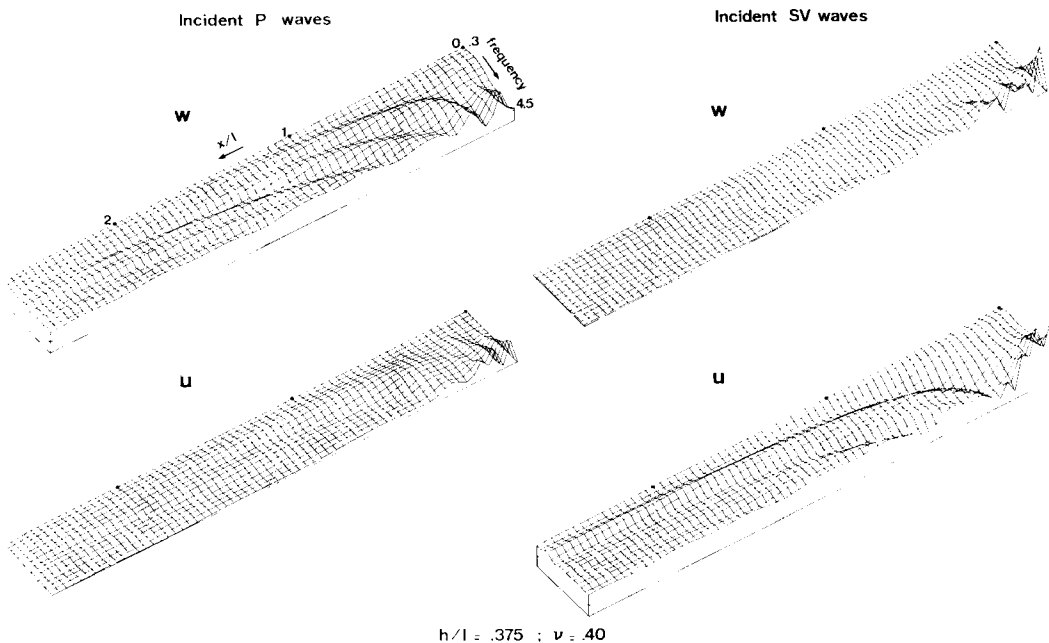

Figure 17. Displacement amplitude as a function of site location and frequency for the large Poisson ratio case ($\nu = 0.40$), and for incident P-waves (left) and SV-waves (right). The top diagrams represent the vertical component, and the bottom diagrams the horizontal component.

The displacement field over the anomaly itself also exhibits significant variations. On the mountain top, the overall shape of the spectrum remains roughly the same in both cases for both P and SV incident waves, but the high-frequency deamplification in the P incident case is much more important for $\nu = 0.40$ (up to 70 per cent for $\eta = 4.0$), and for incident SV-waves, the amplification is always greater when $\nu = 0.40$. These features may be explained by the changes in energy focusing, which is smaller in the former case and greater in the latter, because of the variations in the propagation direction of the reflected SV- and P-waves, respectively.

On mountain flanks, the spectrum shape of the main component of displacement (i.e. the vertical for incident P-waves, and vice versa), remains roughly similar, but differential motions are greater, for incident P-waves, for $\nu = 0.25$ and, in the SV incident case, for $\nu = 0.40$ (that is, the amplification is greater on the mountain top, and deamplification greater near the base). Nevertheless, these differential strains are in some sense balanced by the other component of motion, which is higher for $\nu = 0.40$ in the P incident cases and vice versa for incident SV-waves.

3 Topographies having a more complex geometric shape

The above reported results only deal with isolated topographic features, having a rather simple and smooth geometric shape. Unfortunately, such cases are met in nature only very occasionally, and topographic features most often either present a pronounced three-dimensional character, the investigation of which is beyond our present purpose, or, when roughly two-dimensional, consist of a complex alternation of mountains and valleys of quite different heights, slopes and widths. Of course, a theoretical study such as the present one cannot include every particular case that may occur in reality; notwithstanding, it is
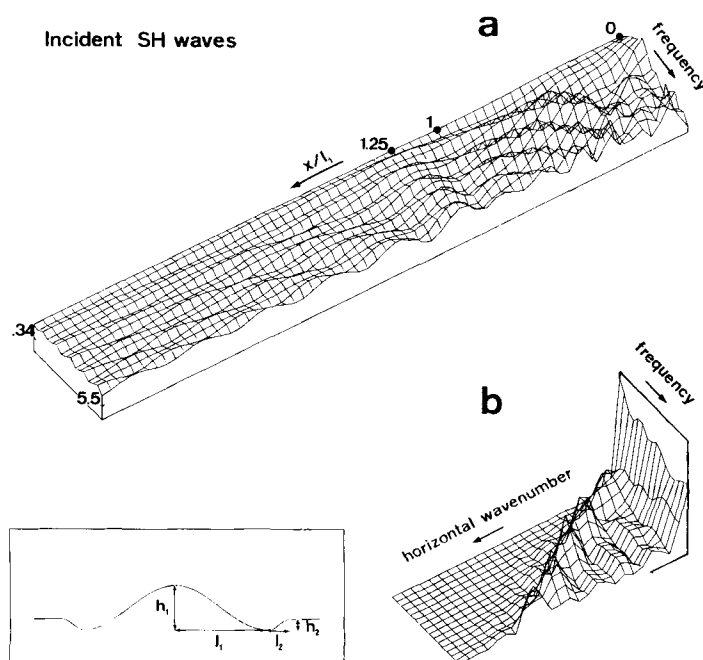

Figure 18. Displacement field and wavefield characteristics for the topographic structure illustrated in the bottom left box, and specified in the text. (a). Displacement amplitude as a function of site location and frequency. (b) Scattered waves amplitude as a function of horizontal wavenumber and frequency.

interesting to have some rough ideas about the modifications undergone by the scattered wavefield and the surface motion when the topographic structure has a somewhat higher degree of complexity than the above investigated mountain model.

Fig. 18(b) illustrates the *SH* scattered field of a cosine-shaped mountain of shape ratio $h_1/l_1 = 0.5$, flanked on each side by a small cosine-shaped depression of same shape ratio h_2/l_2. The mountain width is four times the depression width: $l_1/l_2 = 4$. Although this diagram is much more complicated than those shown on Fig. 6, its main characteristic remains the existence of a horizontally diffracted *SH*-wave. The great difference is, however, that its amplitude shows a near dependence on frequency, combined with a strong intensification with respect to the isolated mountain case (up to 3.5 times larger). Moreover, the frequencies at which these high amplitudes occur correspond to integer values of the mountain width over wavelength ratio $2l_1/\lambda$, thus indicating some kind of lateral resonance effect. This great amplitude horizontal *SH*-wave has obviously a strong influence on the displacement field (Fig. 18a), and induces strong differential strains on mountain slopes at much lower frequencies than in the isolated mountain case (Fig. 8a). Furthermore, the low-frequency amplification on the mountain top is greatly enhanced (up to 80 per cent spectral
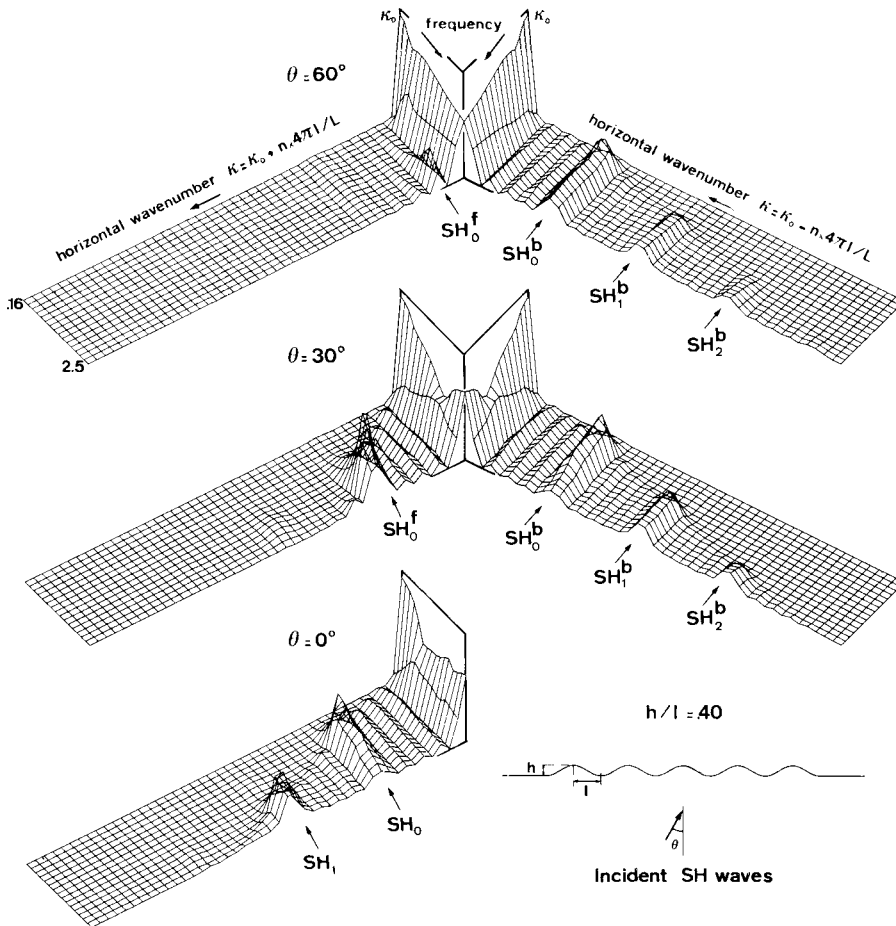

Figure 19. Scattered waves amplitude as a function of horizontal wavenumber and frequency, for the topographic structure illustrated on bottom right corner when impinged by *SH*-waves under various incidence angles. See Fig. 10 and text for further explanations and comments.
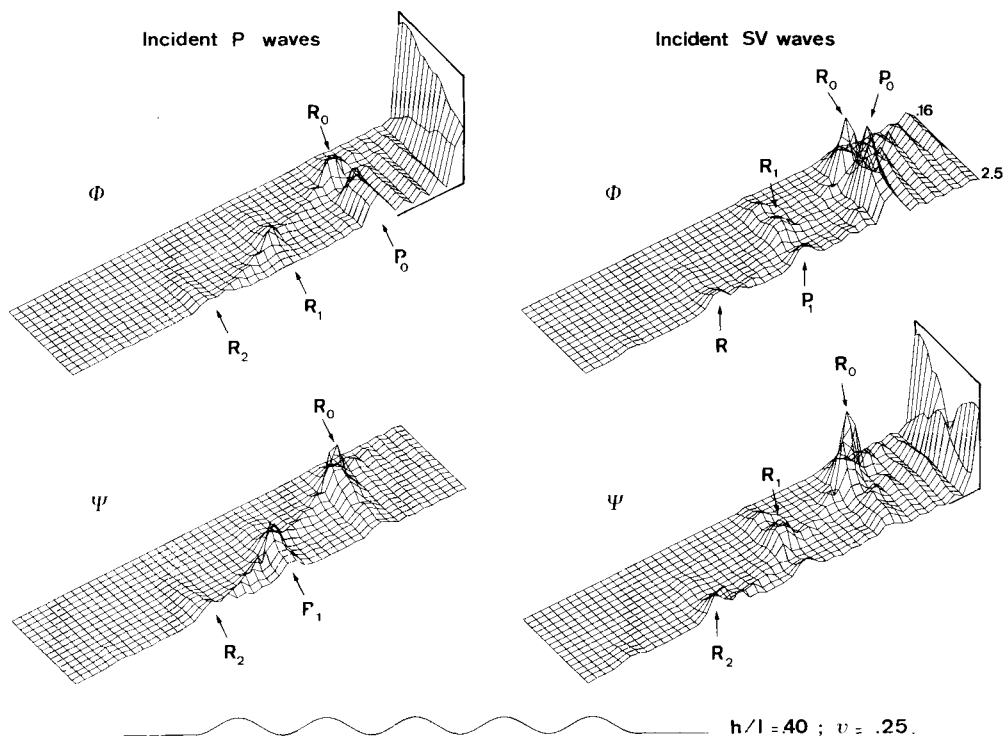
Figure 20. The same as Fig. 5, but for the topographic structure illustrated in Fig. 19.

amplification for $\eta \simeq 2l_1/\lambda \simeq 2$), probably because of a greater energy trapping in the mountain, due to the lateral small depressions.

The frequency-dependent strengthening of the diffracted wave has led us to investigate another topographic feature, involving some kind of periodicity in its geometric shape. Such a case is not unrealistic, since some mountain ranges, such as for instance the Appalachian mountains, exhibit a very clear sequence of two-dimensional ridges and valleys having similar widths and heights. We have chosen a series of five cosine-shaped mountains of the same shape ratio, $h/l = 0.4$.

Figs 19 and 20 present the elastic field scattered by such a topography for vertical and oblique SH-waves, and for vertically incident P- and SV-waves, respectively. The resonance effect mentioned above is now very clear in each case, and affects the three diffracted waves (SH, P and Rayleigh). The corresponding frequencies are $f_n = (n+1) \cdot c/2l$ (where c is respectively β, α and $c_R = 0.92\beta$) in the vertical incidence case. They are shifted for the SH oblique incidence cases, according to the relation:

$$f_n = (n+1) \frac{\beta}{2l} \frac{1}{1 + \epsilon \sin\theta} \qquad \text{with} \qquad n = 0, 1, 2, \ldots$$

$\epsilon = -1$ for the forward scattered wave $SH_n^f (f_n^f)$,

$\epsilon = +1$ for the backward scattered wave $SH_n^b (f_n^b)$.

This equation may be derived in a straightforward way from a constructive interference pattern between waves diffracted at the different ridges. In the oblique incidence case, the backward scattered wave appears therefore at much lower frequencies than the forward

scattered wave:

$$\frac{f_n^{\mathrm{f}}}{f_n^{\mathrm{b}}} = \frac{1 + \sin\theta}{1 - \sin\theta} \ .$$

Moreover, the diffracted wave strengthening at resonance frequencies is particularly strong, since their amplitude is up to 5 times greater than in the case illustrated in Figs 3 and 4.

The detailed examination of these diagrams displays some complementary features. First, in each case, the amplitude of the scattered field shows a peak around

$$k = 2\pi \cdot \frac{n+1}{2l} \cdot \frac{1}{1 + \epsilon \sin\theta},$$

for frequencies higher than the corresponding resonance frequency f_n: the resonance thus also affects the obliquely scattered waves. However, the weakening of this peak with increasing frequency indicates that this effect is maximum on the horizontally diffracted waves.

Furthermore, the 'fundamental' resonance gives rise in each case to larger amplitude for the corresponding diffracted wave than the 'higher' modes. This feature is particularly enhanced for the Rayleigh wave in the SV case, where the second resonance is very weak.
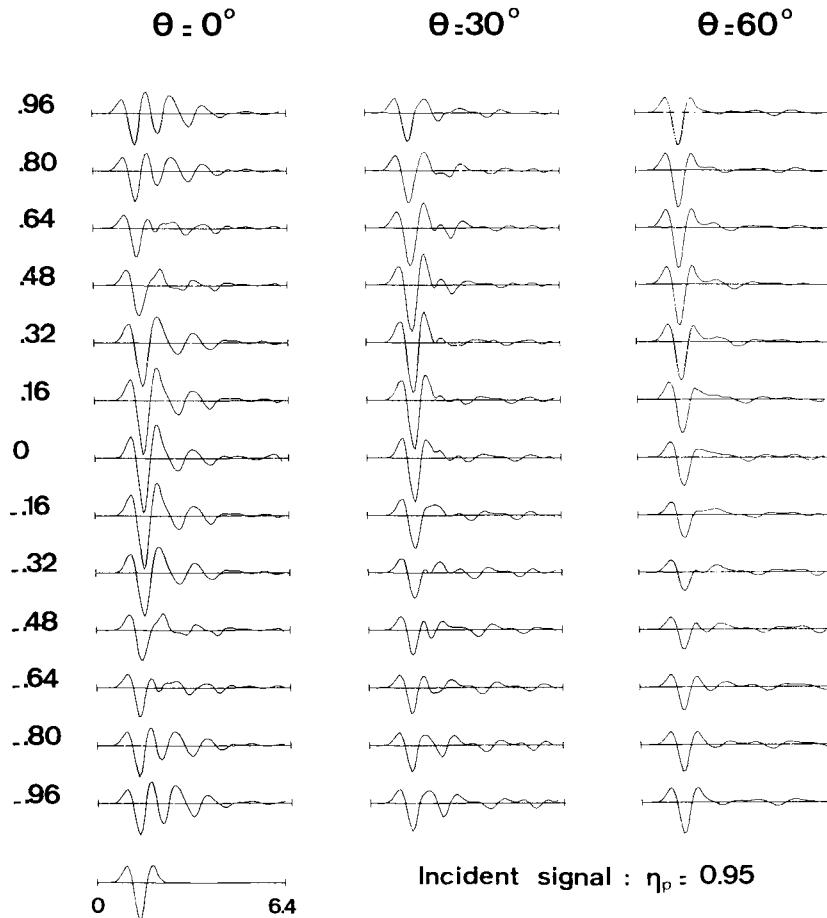

Figure 21. Response of the topographic structure illustrated in Fig. 19 to an SH Ricker wavelet of characteristic frequency 0.95, incident under various angles. The ground motion is shown only for the central hill because of the structure periodicity.

This may perhaps be related with the above mentioned vanishing of the diffracted Rayleigh wave for dimensionless frequencies between 1.5 and 2.5.

Finally, as to the dependence of the diffracted waves both on wave type and incidence angle, these diagrams confirm what might be inferred from previous sections. The *SV*-waves still possess the larger scattering power (at least for the fundamental mode), especially for the diffracted *P*-wave: its amplitude in the *SV* case is more than twice that in the *P* case,
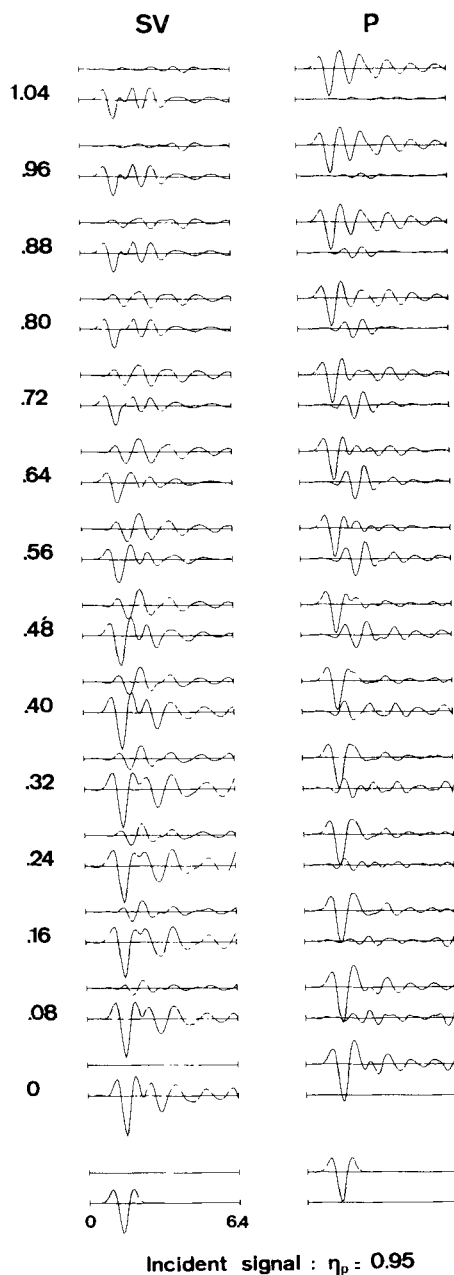
Figure 22. Response of the topographic structure illustrated in Fig. 19 to vertically incident *SV* and *P* Ricker wavelets of characteristic frequency 0.95. As in Fig. 21, the ground motion is computed only over the central hill.

while the fundamental Rayleigh wave is 50 per cent larger for incident *SV*-waves too. From another point of view, the amplitude of the backward scattered *SH*-wave diminishes as the incidence angle increases, and the contrary for the forward scattered wave. One may reasonably think that the diffracted waves follow a similar behaviour for obliquely incident *P*-waves.

The time response of such a topography is illustrated in Fig. 21 for the *SH* cases, and in Fig. 22 for the *P* and *SV* cases. The synthetic seismograms are shown only over the central hill because the topography periodicity induces a strong periodicity in the displacement field (the only difference is that motion lasts somewhat longer on the lateral hills than on the central one).

A common striking feature is the strong prolongation of the displacement duration. This property results from the arrival of the waves scattered at each hill. As seen in Fig. 21, this prolongation lessens as the incidence angle increases. Nevertheless, as the resonance frequencies are considerably shifted for obliquely incident waves, we may think that the duration may be longer for oblique waves in the case of high-frequency incident signals. However, for the particular incident signal investigated here, the main scattered waves in the oblique *SH* cases appear very clearly to be the back scattered ones.

The displacement amplitude variations over the topography are still much greater in the *S* cases than in the *P* case. In the vertical incidence case, the amplification always occurs on the mountain top (+43 per cent in the *SH* case, +33 per cent in the *SV* case, and +20 per cent in the *P* case), but the location of maximum deamplification differs according to the incident wave type: in the *SV* and *P* cases, these are valleys (−37 per cent and −8 per cent, respectively), whereas they are hill slopes in the *SH* cases (−25 per cent at mid-slope). In each case, the differential motion is the most important on mountain slopes, because of the rapid frequency and amplitude changes in the displacement field. This appears very clearly in the *SH* case.

In the case of oblique incident waves, the results follow what has been found for simple topographies. The near side undergoes increasing deamplification when the incidence angle increases, and so does the maximum amplification, shifted on the far side, with increasing incidence angle.

In conclusion, we think that the complexity of the topography has little effect on the primary wave amplitude, but it significantly prolongates and complicates the end of the signal because of the number and amplitude of scattered waves. This may be important for complex and long incident signals, for which scattered and direct waves may strongly interfere.

Such interferences may explain the considerable scatter in experimental data, such as those of Griffiths & Bollinger (1979), for which the surrounding topography (Appalachian Mountains) actually exhibits some kind of two-dimensional periodicity, as assumed here. Anyhow, our results fail to explain the large amplification values they generally observed for the crest/base or crest/slope amplitude ratios in the time domain.

4 Conclusion

The Aki-Larner technique has been used to perform, in both the time and frequency domains, a circumstantial analysis of the effects of two-dimensional topographies on ground motion. Incident plane *SH-*, *SV-* and *P*-waves, having wavelengths comparable with the horizontal and vertical sizes of the topographic feature and longer have been considered. The respective influences of the surface geometry, of the elastic parameters of the half-space and of the incident wave characteristics, have been investigated in some detail, to get a clear view of the physics of the topographic effects.

Essentially two such effects, both appearing at very long wavelengths (about four times the topographic width), show up for the topographic structures investigated in this paper: the first concerns the now classical amplification/deamplification pattern, related to the local surface curvature, and the second consists of a wave diffraction scheme on the convex parts of the topography.

The well-known amplification on mountain top is observed in each of the three SH, SV and P cases; its amount is more important for incident S-waves than for P-waves, which is consistent with the experimental observations of Davis & West (1973), and Griffiths & Bollinger (1979). Yet this amplification does not occur systematically, and it is shown to depend significantly on the characteristics of both the incident waves and the topographic structure. Although this dependence may vary from one case to another (and especially for incident SV-waves), the following features are generally observed: the amplitude spectrum exhibits a rather flat maximum for wavelengths comparable with, or slightly shorter than the mountain width; this amplification generally decreases with increasing incidence angle (and SV-waves incident at the critical angle give rise to a significant deamplification on mountain tops), it increases with mountain height, at least for the rather smooth topographies investigated here, and it also shows a significant but complex dependence on the Poisson ratio. This amplification scheme is obviously replaced by a deamplification one for concave topographies, but we did not investigate this latter case in detail.

The other effect of topographic irregularities is the diffraction of body and surface waves, which are generated on the convex parts of the topography and then propagate outwards along the ground surface. The type and the amplitude of these waves depend on the incident wave type. In the SH case, we observe a horizontally diffracted SH-wave; in the P case, we have mainly a Rayleigh wave, with a weak horizontal P-wave; in the SV case, both P- and Rayleigh-waves are present and their amplitude may be very large for some values of the frequency and/or the incidence angle. Incident SV-waves clearly possess the greatest scattering power, and seem to be associated with the most complicated diffraction scheme. Whereas intuitive reasoning concerning the behaviour of the diffracted waves (strengthening as mountain height increases, rather smooth frequency dependence, strengthening of the forward scattered waves and weakening of the back scattered as incidence angles increases) agree quite well with the computed results in both SH and P cases, they completely fail for incident SV-waves. This particular behaviour, together with the large amplitude of the scattered P-wave in the SV case, should, in our opinion, be related with the importance and the sensitivity of the S–P reflections, as previously underlined by Bouchon (1978) and Bard & Bouchon (1980b). These scattered waves control the displacement field over a wide area around the topographic irregularity, and may be of great importance in earthquake engineering studies. For instance, their lateral propagation along mountain slopes, as well as their interference with the primary wave, may result in strong differential strain, over distances and for frequencies in the range of man-made structures. For complex topographies (which is the general case), the large number of scattered waves may result in a significant prolongation of the ground motion.

In conclusion, it must be underlined that, in spite of the extreme simplicity of the geometrical models investigated here, the topographic effects exhibit a great complexity due to their dependence on the incident wave characteristics. From the results presented in this paper, it is thus very difficult to infer general rules concerning the displacement field over topographic irregularities. Moreover, real topographies may be affected by other phenomena than those treated in the present study: for instance, steeper topographies may give rise to a lateral resonance pattern making the topographic structure oscillate as a whole. In other respects, the two-dimensional assumption, which is only seldom met with in reality, may lead to an underestimation of the actual topographic effects, especially those affecting the

primary wave amplitude. Finally, another important factor may be the presence of layering under the topographic structure, which, in our opinion, may enhance the amplitude of the scattered body *SH*- or *P*-waves by converting them into Love or Rayleigh waves. Such effects could perhaps explain the quantitative discrepancy which still exists between the numerous theoretical results and the experimental observations.

References

Aboudi, J., 1971. The motion excited by an impulsive source in an elastic half-space with a surface obstacle, *Bull. seism. Soc. Am.,* **61**, 747–763.

Aki, K. & Larner, K. L., 1970. Surface motion of a layered medium having an irregular interface due to incident plane *SH* waves, *J. geophys. Res.,* **75**, 933–954.

Alterman, Z. A. & Aboudi, J., 1971. Propagation of elastic waves caused by an impulsive source in a half-space with a corrugated surface, *Geophys. J. R. astr. Soc.,* **24**, 59–76.

Alterman, Z. A. & Nathaniel, R., 1975. Seismic waves in a wedge, *Bull. seism. Soc. Am.,* **65**, 1697–1719.

Bard, P.-Y. & Bouchon, M., 1980a. The seismic response of sediment-filled valleys. Part 1. The case of incident *SH* waves, *Bull. seism. Soc. Am.,* **70**, 1263–1286.

Bard, P.-Y. & Bouchon, M., 1980b. The seismic response of sediment-filled valleys. Part 2. The case of incident *P* and *SV* waves, *Bull. seism. Soc. Am.,* **70**, 1921–1941.

Boore, D. M., 1972. A note on the effect of simple topography on seismic *SH* waves, *Bull. seism. Soc. Am.,* **62**, 275–284.

Bouchon, M., 1973. Effect of topography on surface motion, *Bull. seism. Soc. Am.,* **63**, 615–632.

Bouchon, M., 1978. The importance of the surface or interface *P*-wave in near earthquake studies, *Bull. seism. Soc. Am.,* **68**, 1293–1311.

Davis, L. L. & West, L. R., 1973. Observed effects of topography on ground motion, *Bull. seism. Soc. Am.,* **63**, 283–298.

England, R., Sabina, F. J. & Herrera, I., 1980. Scattering of *SH* waves by surface cavities of arbitrary shape using boundary methods, *Phys. Earth planet. Int.,* **21**, 148–157.

Gilbert, F. & Knopoff, L., 1960. Seismic scattering from topographic irregularities, *J. geophys. Res.,* **65**, 3437–3444.

Griffiths, D. W. & Bollinger, G. A., 1979. The effect of Appalachian mountain topography on seismic waves, *Bull. seism. Soc. Am.,* **69**, 1081–1105.

Hudson, J. A., 1967. Scattered surface waves from a surface obstacle, *Geophys. J. R. astr. Soc.,* **13**, 441–458.

Hudson, J. A. & Boore, D. M., 1980. Comments on 'Scattered surface waves from a surface obstacle', *Geophys. J. R. astr. Soc.,* **60**, 123–127.

Hudson, J. A. & Knopoff, L., 1967. Statistical properties of Rayleigh waves due to scattering by topography, *Bull. seism. Soc. Am.,* **57**, 83–90.

Ilan, A., 1977. Finite difference modelling for *P*-pulse propagation in elastic media with arbitrary polygonal surface, *J. Geophys.,* **43**, 41–58.

Ilan, A., Bond, J. L. & Spivack, M., 1979. Interaction of a compressional impulse with a slot normal to the surface of an elastic half-space, *Geophys. J. R. astr. Soc.,* **57**, 463–477.

Key, F. A., 1967. Signal generated noise recorded at the Eskdalemuir seismometer array station, *Bull. seism. Soc. Am.,* **57**, 27–37.

Larner, K. L., 1970. Near receiver scattering of teleseismic body waves in layered crust–mantle models having irregular interfaces, *PhD thesis,* Massachusetts Institute of Technology, Cambridge.

McIvor, I. K., 1969. Two-dimensional scattering of a plane compressional wave by surface imperfection, *Bull. seism. Soc. Am.,* **59**, 1349–1364.

Nason, R. D., 1971. Shattered earth at Wallaby Street, Sylmar, *Prof. Pap. US geol. Surv.*, **733**, 97–98.

Rogers, A. M., Katz, L. J. & Bennett, T. J., 1974. Topographic effects of ground motion for incident *P* waves – a model study, *Bull. seism. Soc. Am.*, **64**, 437–456.

Sabina, F. J. & Willis, J. R., 1975. Scattering of *SH* waves by a rough half-space of arbitrary slope, *Geophys. J. R. astr. Soc.*, **42**, 685–703.

Sabina, F. J. & Willis, J. R., 1977. Scattering of Rayleigh waves by a ridge, *J. Geophys.*, **43**, 401–419.

Sanchez-Sesma, F. J. & Rosenblueth, E., 1979. Ground motion at canyons of arbitrary shape under incident *SH* waves, *Int. J. Earthq. Eng. Struct. Dyn.*, **7**, 441–450.

Sills, L. B., 1978. Scattering of horizontally polarized shear waves by surface irregularities, *Geophys. J. R. astr. Soc.*, **54**, 319–348.

Singh, S. K. & Sabina, F. J., 1977. Ground motion amplification by topographic depressions for incident *P* waves under acoustic approximation, *Bull. seism. Soc. Am.*, **67**, 345–352.

Smith, W. D., 1975. The application of finite element analysis to body wave propagation problems, *Geophys. J.*, **42**, 747–768.

Trifunac, M. D., 1973. Scattering of plane *SH* waves by a semi-cylindrical canyon, *Int. J. Earthq. Eng. Struct. Dyn.*, **1**, 267–281.

Trifunac, M. D. & Hudson, D. E., 1971. Analysis of the Pacoima Dam accelerogram. San Fernando, California, earthquake of 1971, *Bull. seism. Soc. Am.*, **61**, 1393–1411.

Wong, H. L. & Jennings, P. C., 1975. Effect of canyon topography on strong ground motion, *Bull. seism. Soc. Am.*, **65**, 1239–1257.

Wong, H. L. & Trifunac, M. D., 1974. Scattering of plane *SH* waves by a semi-elliptical canyon, *Int. J. Earthq. Eng. Struct. Dyn.*, **3**, 157–169.